https://dx.doi.org/10.21577/0103-5053.20220015

J. Braz. Chem. Soc., Vol. 00, No. 00, 1-10, 2022

Article

Boosting the Photocurrent of the $WO_3/BiVO_4$ Heterojunction by Photoelectrodeposition of the Oxy-Hydroxide-Phosphates Based on Co, Fe, or Ni

Dyovani Coelho, *,[a] *João Pedro R. S. Gaudêncio*[a] *and Lucia H. Mascaro* *,[a]

[a]*Laboratório de Materiais Nanoestruturados Fabricados Eletroquimicamente, Departamento de Química, Universidade Federal de São Carlos (UFSCar) 13565-905 São Carlos-SP, Brazil*

Here we investigated the photoelectrodeposition of oxygen-evolving catalysts (OECs) based on oxy-hydroxides-phosphates of Co, Fe, or Ni (CoPi, FePi, and NiPi) on the $WO_3/BiVO_4$ heterojunction and their activity in water oxidation. The OECs were deposited by cycles of (*i*) open-circuit potential (OCP) and (*ii*) applying a potential positive enough to oxidize the metallic precursor on the $WO_3/BiVO_4$. The crystalline and optical properties of the photoanodes were not significantly affected by the OECs deposition. However, there was a remarkable increase in the photocurrent densities (j_{pc}) to water oxidation, where the modification with FePi showed the best result, achieving 2.12 mA cm^{-2}, which corresponds to 2.83 times higher than the heterojunction without the OECs. Furthermore, the OECs deposition changed the morphology of the heterojunction with the deposition of a thin film on its surface. In addition, during the FePi deposition, the $BiVO_4$ layer seems to partially dissolve. Our study shows a facile methodology to boost the activity of photoanodes to the water oxidation by photoelectrodeposition of OECs.

Keywords: $BiVO_4$, WO_3, oxygen-evolving catalyst, water splitting, oxy-hydroxides metals

Introduction

The direct conversion of solar light into useful energy can be achieved in two ways, by converting light into electricity with photovoltaic cells or by converting light into useful chemical energy such as the decomposition of water into H_2 and O_2.[1-3] This conversion into solar fuel, such as H_2, is widely known as water splitting and has gained prominence in recent years due to the new semiconductor materials design and the environmental appeal. Water splitting is one of the most interesting, renewable, and sustainable systems because the combustion of O_2 and H_2 yields H_2O and energy as byproducts.[1,4]

The use of sunlight for the production of H_2 and O_2 from the decomposition of water is based on the use of semiconductors such as photoanodes (n-type semiconductors responsible for the production of O_2) and/or photocathodes (p-type semiconductors responsible for the production of H_2) and requires a relatively simple device.[5] In general, a transparent photocell to solar radiation, a light absorber (photoanode and photocathode), electrocatalysts for the formation of solar fuel, electrolyte, and a way to separate the products (O_2 and H_2).[3] However, the oxygen evolution reaction (OER) is harder than the hydrogen evolution reaction (HER) due to the requirement of several steps of electrons and protons transfer to the production of one O_2 molecule. The several steps turn the OER kinetics sluggish, which results in a large overpotential to obtain a significant amount of product.[6] Thus, the investigation of efficient and stable photoanodes is pivotal to the development of this technology, furthermore, the bandgap and valence and conduction band alignment of the light absorbent material are critical to OER.[7] These requirements turn the $BiVO_4$ a good choice to put effort.

$BiVO_4$ is an n-type semiconductor with three crystalline phases, monoclinic scheelite, tetragonal, and zircon-type, and presents bandgap energy between 2.4 and 2.9 eV. The monoclinic phase presents a high photocatalytic activity due to the low bandgap (2.4 eV), which allows a high visible light harvesting too.[8] In addition, the valence band edge potential of the $BiVO_4$ is more positive than the O_2/H_2O redox couple, so the water oxidation can occur spontaneously on the semiconductor surface under illumination, apart from being stable in neutral or slightly acidic or alkaline solution.[9,10] However, the $BiVO_4$ lacks charge diffusion length (ca. 80 nm) and mobility (ca. 10^{-2} cm^2 V^{-1} s^{-1}), which causes a high recombination rate of electron-holes.[11-13] Consequently, some strategies are used to compensate for the charge transport deficiency

*e-mail: dyovani@gmail.com; lmascaro@ufscar.br
Editor handled this article: Teodoro S. Kaufman

as doping, the heterojunction production, and the OECs deposition on its surface.[8,14-16] The use of WO_3 to produce heterojunctions with $BiVO_4$ has been largely investigated due to band levels' alignment of the valence and conduction band and because of its better electric properties compared to the latter. The WO_3 valence and conduction band are more positive than those of $BiVO_4$, which allow the prompt charge transfer between the semiconductor layers, in addition, the charge diffusion length to WO_3 is ca. 500 nm and the charge mobility is ca. 5 $cm^2 V^{-1} s^{-1}$, which enable fast charge transport into the semiconductor.[17]

Regarding the OECs, they are useful to decrease the charge transfer resistance in the interface photoanode-electrolyte, namely, to decrease the activation energy to water oxidation.[18] Thus, the OEC has to be stable and present high catalytic activity, consequently, noble metal oxides as IrO_2 and RuO_2 are used to drive the OER, but their high cost is prohibitive in commercial devices.[19-21] As an alternative, earth-abundant transition metal oxy-hydroxides based on Fe, Ni, and Co have been received much attention to reduce or even eliminate the use of noble metals to OER.[6,7] These oxy-hydroxides, as FeOOH, NiOOH and Co_3O_4 have been applied in both electro- and photoelectrochemical OER.[4-6,22-26]

Focusing on photoelectrochemical OER using $BiVO_4$ as a light-absorbing layer there are results very interesting. Chhetri *et al.*[27] reported the use of Co-La double hydroxide and reached photocurrent densities (j_{pc}) 2.7 times higher than pristine photoelectrode at 1.23 V *vs.* reversible hydrogen electrode (RHE) into 0.5 mol L^{-1} phosphate buffer pH 7. Wang *et al.*[28] employed two steps of photoelectrodeposition to obtain $CoFeO_x$ on $BiVO_4$, in the optimal conditions, the photoanode exhibits a j_{pc} of 4.82 mA cm^{-2} at 1.23 V *vs.* RHE, which represented an increase of ca. 2.1 times related to non-modified material. In another way, Shi *et al.*[29] doped the $BiVO_4$ with Mo and covered the surface of photocatalyst with a tannic acid coordinated with Ni and Fe ions, which yielded j_{pc} of 5.10 mA cm^{-2} at 1.23 V *vs.* RHE into 0.5 mol L^{-1} sodium borate buffer pH 8.5, while the only doped $BiVO_4$ showed 2.89 mA cm^{-2}. The use of FeOOH as OEC was tested by Seabold *et al.*[30] and showed an increase of ca. 82 times if compared to pristine $BiVO_4$, achieving 1.65 mA cm^{-2} at 1.2 V *vs.* RHE into 0.1 mol L^{-1} KH_2PO_4 pH 7. Also, Kim *et al.*[31] described the application of a mixture of FeOOH and NiOOH as OEC, which exhibited remarkable stability at 0.6 V *vs.* RHE into phosphate buffer pH 7 over 40 h with j_{pc} around 2.6 mA cm^{-2}. On the other hand, cobalt phosphate has been used with success to OEC on $BiVO_4$ too. After cobalt phosphate (CoPi) deposition on pristine $BiVO_4$ and W-doped $BiVO_4$, Abdi *et al.*[32,33] showed an increase around 3 times in the j_{pc} at 1.2 V *vs.* RHE into 0.1 mol L^{-1} phosphate buffer pH 7, if compared with CoPi non-modified photoelectrode.

Here, we investigate the obtainment of the $WO_3/BiVO_4$ heterojunction employing spray deposition, electrodeposition, and heat treatment, besides, its modification with the OECs based on Co, Fe, or Ni by the use of a simple photoelectrodeposition methodology. Furthermore, we demonstrated that the photoelectrodeposition of OECs based on Co, Fe, or Ni, affects the $BiVO_4$ morphology in different ways, which reflects in the j_{pc} and stabilities for long-term too.

Experimental

Reagents

All chemicals were purchased from Sigma-Aldrich/Merck (St. Louis, USA) at analytical grade (used without further purification) and then maintained at room temperature (ca. 25 °C). Moreover, solutions were prepared with deionized water (resistivity of 18.2 MΩ cm, Millipore®, Billerica, USA). The salts used as precursors were $Bi(NO_3)_3.5H_2O$ (98.0%), NH_4VO_3 (99.0%), $Co(NO_3)_2.6H_2O$ (98.0%), $Ni(NO_3)_2.6H_2O$ (98.5%), $Fe(NO_3)_3.9H_2O$ (98.0%), $(NH_4)_{10}H_2(W_2O_7)_6$ (99.99%), ethylene glycol (99.8%), poly(ethylene glycol) 300 (Kollisolv® PEG E 300), $NaClO_4$ (98.0%), Na_2HPO_4 (99.0%), Na_2SO_4 (99.0%), and H_3PO_4 (85 wt.% in H_2O).

The 0.1 mol L^{-1} Na_2HPO_4 pH 7.0 and 0.1 mol L^{-1} Na_2HPO_4 + 0.5 mol L^{-1} Na_2SO_4 pH 7.0 solutions were prepared dissolving the salt into deionized water and adjusting the pH with 1.0 mol L^{-1} H_3PO_4.

Preparation of $WO_3/BiVO_4$ heterostructure

The $WO_3/BiVO_4$ heterostructure was obtained by the methodology described by Coelho *et al.*[10] with modifications. Briefly, the WO_3 layer was deposited on FTO (fluorine-doped tin oxide coated glass, surface resistivity ca. 7 Ω cm, containing an FTO layer around 550 nm thickness and a total thick of 2.2 mm, Sigma-Aldrich, St. Louis, USA) by spray coating using an airbrush (BC 61-03, Forusi®, São Paulo, Brazil) with 10 L min^{-1} and 2 mL min^{-1} of air and solution flows, respectively. The time of spray was 0.25 s and the substrate was kept at 100 °C in 15 cm far from the airbrush nose. The precursor solution was $(NH_4)_{10}H_2(W_2O_7)_6$ 0.002 mol L^{-1} dissolved in a mix of ethylene glycol:H_2O 1:1 (v:v). The interval between each spray deposition was 120 s, and after 40 repetitions the substrates were heat-treated at 500 °C for 60 min. Next, a metallic Bi layer

was electrodeposited on a WO_3 film previously produced using an electrolyte freshly prepared and composed of 0.02 mol L^{-1} $Bi(NO_3)_3$ + 0.1 mol L^{-1} $NaClO_4$ dissolved in poly(ethylene glycol) 300. The Bi electrodeposition was carried out at room temperature and magnetic stirring with 10 cycles of open-circuit potential (OCP) for 60 s followed by applying –1.85 V *vs.* Ag/AgCl/KCl saturated (Ag/AgCl) until charge density of –0.05 C cm^{-2} was reached. This process was performed in a three-electrode configuration cell, being WO_3 coating on FTO substrate, Pt foil, and Ag/AgCl as working, counter, and reference electrodes, respectively. After that, the Bi film was turned into $BiVO_4$ by a conversion step which was performed by dropping 50 µL cm^{-2} of 0.2 mol L^{-1} NH_4VO_3 on Bi film and heat-treating at 500 °C for 1 h in a heating rate of 2 °C min^{-1}. The excess of V_2O_5 was dissolved by immersion in a stirred solution of NaOH 1.0 mol L^{-1} for 5 min and then the photoanodes were rinsed thoroughly with water. Figure 1 shows the sequence of steps to obtain the $WO_3/BiVO_4$ heterostructure.

OECs photoelectrodeposition

The photoelectrodeposition (PED) of OEC's based on oxy-hydroxides phosphates of cobalt, nickel, and iron on $WO_3/BiVO_4$ surface was carried out using a three-electrode configuration cell as that used for Bi electrodeposition, the only difference was at the working electrode, which, here, was the $WO_3/BiVO_4$ heterojunction. The PED was performed into 0.1 mol L^{-1} Na_2HPO_4 pH 7.0 (adjusted with 1.0 mol L^{-1} H_3PO_4) containing 0.5 mmol L^{-1} $M_x(NO_3)_y$ ($M = Ni^{II}$, Co^{II}, or Fe^{III}). The potential to PED was chosen from cyclic voltammetry experiments. The pulse of electrodeposition was limited to a charge of 2.0 mC cm^{-2} $pulse^{-1}$ and there was a relaxing time of 10 s keeping the system in OCP after each pulse. The number of catalyst PED cycles and illumination condition were optimized based on the j_{pc} reached at 1.23 V *vs.* RHE.

Photoelectrochemical characterization

The photoelectrochemical characterizations were performed in a three-electrode cell with the photoanodes, Pt foil, and Ag/AgCl as working, auxiliary, and reference electrodes, respectively. It was used a potentiostat/galvanostat PGSTAT302N from Methrom Autolab BV (Utrecht, Netherlands). The light source was an LCS-100 Solar Simulator (xenon lamp 100 W, filter AM 1.5 G, the irradiance of 100 mW cm^{-2}, model 94011A-ES, Newport®, Irvine, USA). The electrolyte was 0.1 mol L^{-1} Na_2HPO_4 + 0.5 mol L^{-1} Na_2SO_4, pH 7.0. All measurements were carried out at room temperature. The geometric area of the photoanode exposed to electrolyte was approximately 1.0 cm^2. The Ag/AgCl electrode potential was converted to RHE by Nernst equation:

$$E_{RHE} = E_{Ag/AgCl} + E^{\circ}_{Ag/AgCl} + (0.059 \times pH) \quad (1)$$

where E_{RHE} is the potential *vs.* RHE, $E^{\circ}_{Ag/AgCl}$ is 0.197 V at 25 °C, $E_{Ag/AgCl}$ is the potential *vs.* Ag/AgCl measured and pH is 7.0.

Microstructural and optical characterization

The crystallinity of the materials was investigated by X-ray diffraction (XRD, D/Max-2500PC diffractometer, Rigaku Corporation, Tokyo, Japan) with Cu Kα radiation (λ = 0.154184 nm), angle of diffraction 2θ ranging from 10° to 110°, and a scanning step of 0.02° min^{-1}. The morphology was characterized by high-resolution field emission scanning electron microscopy (FE-SEM, Supra 35 at 5 kV, Carl Zeiss AG, Jena, Germany). The

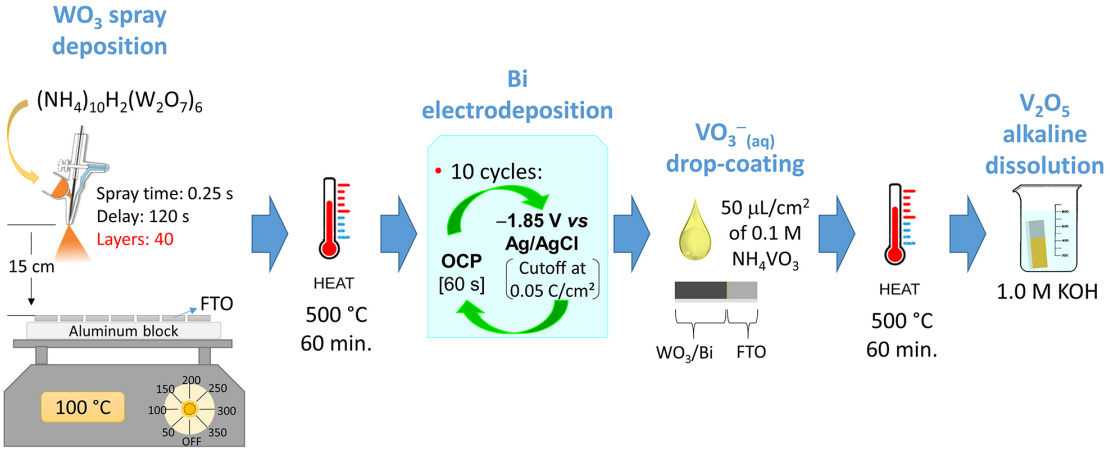

Figure 1. Scheme of the methodology used to obtain the $WO_3/BiVO_4$ heterojunction.

optical properties were analyzed by diffuse reflectance spectroscopy using a UV-Vis-NIR spectrophotometer coupled with an integrating sphere (DRS, Cary 5G, Varian, Palo Alto, USA). Moreover, the samples were characterized by micro-Raman spectroscopy with an exposure time of 30 s and an accumulation of 100 spectra (532 nm He-Cd laser, 50 mW, coupled to an Olympus BX41 microscope and charge-coupled device (CCD) detector, Horiba HR 550 spectrometer, Kyoto, Japan).

Results and Discussion

To understand the deposition behavior of the proposed catalysts on the heterojunction of $WO_3/BiVO_4$, first, their voltammetric profiles were analyzed. Figure 2 shows the heterojunction behavior before and after adding the metallic ions, Co^{II}, Ni^{II}, or Fe^{III} into the electrolyte to determine the deposition potential to be used for their PED. As shown in Figure 2a, in the presence of Co^{II} into solution, an oxidation process is observed starting at approximately 1.56 V *vs.* RHE, which exhibits a maximum at 1.66 V *vs.* RHE. In addition, it is noted that water oxidation is associated with the oxidation of Co^{II}, which is only observed with the presence of the metal ion in a solution containing phosphate ions too, and is due to the catalytic effect of CoPi for this reaction.[34] Similarly, the voltammetric profile of Ni^{II} is shown in Figure 2c, in which it is observed an oxidative process at approximately 2.31 V *vs.* RHE. Thus, at the potentials close to 1.66 and 2.31 V *vs.* RHE, there is the oxidation of the metallic species Co^{II} to Co^{III} and Ni^{II} to Ni^{III}, as well as *in situ* formations of the catalysts CoPi and NiPi, respectively. The designation of MPi (M = metal) is due to the non-stoichiometric compound produced *in situ* using this methodology. As demonstrated by Kanan and Nocera[34] the electrodeposition of the Co^{II} results in an amorphous compound containing mixtures of Co oxide or hydroxide and phosphate anion. It is believed that the *in situ* PED of Ni^{II} occurs in the same way since the solubility product of $Ni_3(PO_4)_2$ is around 4.7×10^{-32} and $Ni(OH)_2$ is 4.7×10^{-16}.[35] Thus, the simultaneous deposition of Ni oxide and phosphate is plausible, as demonstrated by CoPi PED. Therefore, the potential of 1.66 and 2.31 V *vs.* RHE was defined for CoPi and NiPi electrodeposition, respectively.

Interestingly, the voltammetric profile of the heterojunction $WO_3/BiVO_4$ into the solution containing Fe^{III} indicates the presence of one redox process relative to the Fe^{II}/Fe^{III} (Figure 2b). The reduction wave is observed in the negative potential sweep around 0.20 V *vs.* RHE, resulting from the reduction of the Fe^{III} species to Fe^{II}, whereas the oxidation is observed in the same potential

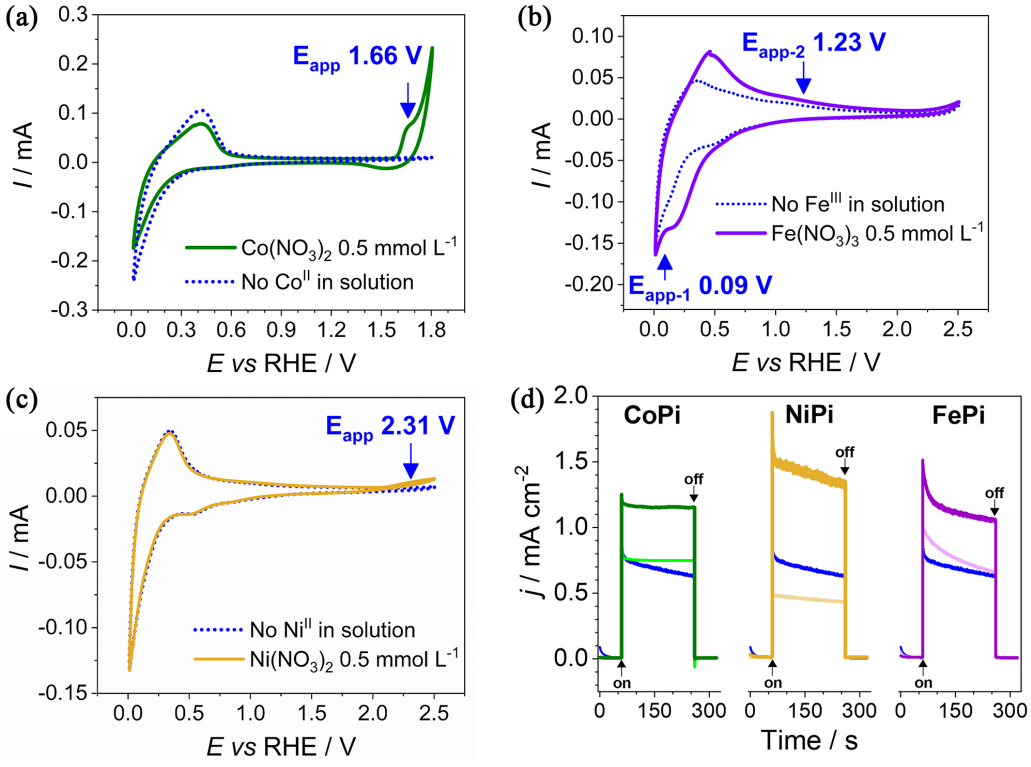

Figure 2. Cyclic voltammetry at 50 mV s^{-1} to $WO_3/BiVO_4$ into 0.1 mol L^{-1} Na_2HPO_4 pH 7.0 containing (a) $Co(NO_3)_2$, (b) $Ni(NO_3)_2$, and (c) $Fe(NO_3)_3$ 0.5 mmol L^{-1}. (d) Chronoamperograms at 1.23 V *vs.* RHE to photoanodes $WO_3/BiVO_4$ after 5 cycles of MPi PED into into 0.1 mol L^{-1} Na_2HPO_4 + 0.5 mol L^{-1} Na_2SO_4 pH 7.0 under solar simulated illumination. Blue line: $WO_3/BiVO_4$, green: CoPi, beige: NiPi, and purple: FePi; strong color: PED under illumination, faded color: PED in dark conditions.

range of the V^{IV}/V^{V}.[36] Thus, to reach the FePi PED were necessary to apply two consecutive pulses, the first at 0.09 V *vs.* RHE and the second at 1.23 V *vs.* RHE since the iron source consisted of Fe^{III} ions. The hypothesis is based on the reduction of Fe^{III} on the photoanode surface and its oxidation *in situ* causing the precipitation of the FePi at the reaction site. The solubility products of the $Fe(OH)_2$, $Fe(OH)_3$, and $FePO_4.2H_2O$ are 4.8×10^{-17}, 2.7×10^{-39}, and 9.9×10^{-16}, respectively, hence the formation of a mix of Fe oxi-hydroxide and phosphate is reasonable.[35] It is noteworthy that the solution pH is around 7.0, so the hydroxyl concentration is ca. 10^{-7} mol L^{-1}, while the hydrogen-phosphate is higher than 0.1 mol L^{-1}.

Based on the voltammetric profile of the heterojunction into an electrolyte containing the metallic precursors, it was defined the electrodeposition of the catalysts CoPi and NiPi as a cycle with two steps: (*i*) keeping the open-circuit potential for 10 s; (*ii*) applying the deposition potential (1.66 V *vs.* RHE to CoPi and 2.31 V *vs.* RHE to NiPi) for the time necessary to reach 2.0 mC cm^{-2}. The OCP step was thought to guarantee a relaxing time to the system in such a way that the concentration of the metallic ions on the photoanode surface could be restored. The PED cycles were repeated as many times as required to increase the catalyst load on heterojunction. To FePi PED, the cycle was modified to three steps: (*i*) OCP for 10 s; (*ii*) 0.09 V *vs.* RHE for 10 s, and (*iii*) 1.23 V *vs.* RHE for the time necessary to reach 2.0 mC cm^{-2}.

Aiming at the application of the photoanode in the decomposition of water, all PED processes were optimized according to the j_{pc} obtained in experiments under incident solar simulated light in a solution containing only the electrolyte (without catalyst precursors dissolved in), after the PED of oxygen evolution catalysts. Then, the effect of the illumination condition during the electrodeposition of metallic phosphates was studied. As shown in Figure 2d, after 5 cycles of catalysts PED, the behavior of the j_{pc} obtained at 1.23 V *vs.* RHE shows better performance under illumination for the three catalysts than those deposited under dark conditions. Actually, to the NiPi deposition, the absence of incident light decreases the j_{pc} if compared to $WO_3/BiVO_4$. The higher j_{pc} is probably due to the preferential deposition of catalysts in the active sites to water oxidation of the heterostructure.[31,37] The catalyst that showed the greatest j_{pc} gain was NiPi (110%), followed by the films containing CoPi (83%) and FePi (66%), all of them deposited under illumination (Figure 3a). The presence of incident light during the PED affects the charge generation in the semiconductor layer by the excitation of electrons from the valence band to the conduction band. As the $WO_3/BiVO_4$ heterojunction is an n-type semiconductor and is positively biased, the holes are driven to the semiconductor-electrolyte interface and help the oxidation of the catalyst on the reaction site. It is believed that the deposition on the reaction site allied to the higher potential of the holes ensures a highly efficient catalyst deposition on the heterojunction surface, which in turn shows higher j_{pc} if compared to de catalyst deposition in dark conditions. Therefore, it was decided to use photoelectrodeposition of metallic phosphates. The number of cycles of the catalyst PED on the $WO_3/BiVO_4$ heterojunction was optimized too (Figure 3b). Given the particular nature of each metallic species, it was expected different optimal procedures for each catalyst. In accord to Figure 3b, the high j_{pc} is obtained with 5, 25, and 50 cycles of catalyst PED to CoPi, NiPi, and FePi, respectively.

Although Faraday's law can be used to access the number of deposited species, the quantitative analysis becomes unfeasible. This is because, under lighting, it is not possible, with the techniques used here, to separate the current originating from the oxidation of metallic ions from that resulting from the oxidation of water. In this context,

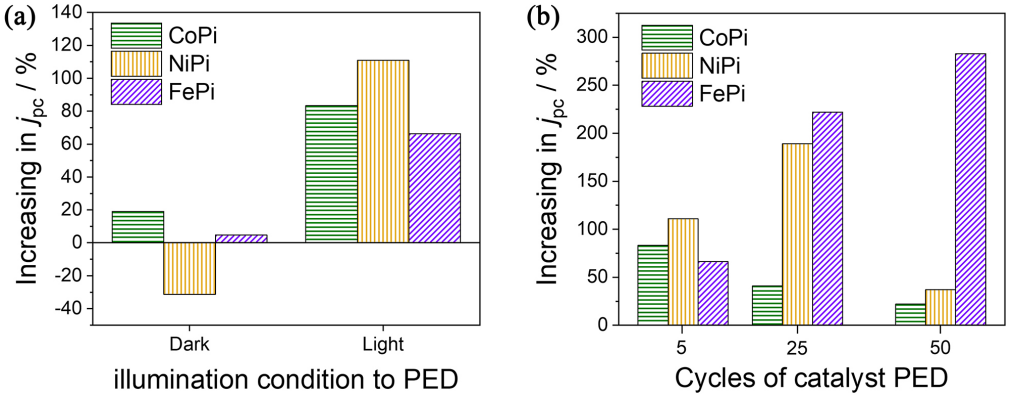

Figure 3. OECs electrodeposition optimization. (a) Increasing in the j_{pc} of the $WO_3/BiVO_4$/OEC with 5 cycles of catalyst PED in dark or incident light conditions relative to $WO_3/BiVO_4$ after 200 s under illumination. (b) Increasing in j_{pc} keeping the OECs PED under incident light and varying the number of PED cycles.

it becomes very complex to evaluate the contribution of each process in the charge consumption and to determine the faradaic efficiency of the deposition.

Figure 4a shows the linear voltammograms of the photoanodes containing WO_3 and $WO_3/BiVO_4$ in comparison with the heterostructure covered by the OEC's under optimized conditions of PED. It can be seen that the j_{pc} obtained at 1.23 V by the pristine WO_3 is 0.22 mA cm^{-2}, while the $WO_3/BiVO_4$ heterojunction presents 0.75 mA cm^{-2}, hence 3.4 times higher than the former. This increase in the j_{pc} corroborates the idea of forming a type-II heterojunction (Staggered gap), which minimizes the formation of alternative paths for the passage of photogenerated charges, thus enabling the effective spatial separation of charges when this is transferred from one layer to another.[38] Under the same conditions, the $WO_3/BiVO_4$/OECs show increase of 1.56, 1.89, and 2.83 times to CoPi (1.17 mA cm^{-2}), NiPi (1.42 mA cm^{-2}), and FePi (2.12 mA cm^{-2}), respectively, related to heterojunction without the catalysts. This significant increase is due to the highest transfer rate of photogenerated holes to water, minimizing the recombination of electron-holes at the semiconductor/electrolyte interface.[4] Thereby, the use of all catalysts proposed here allowed the overcoming of the kinetic barrier generated by the limitation of charge transfer from the electrolyte to the semiconductor.

The stability of the heterojunctions containing the catalysts was investigated for 3600 s with an interval of 30 s of light off each 20 min (Figure 4b). The initial j_{pc} observed to photoanodes were 1.15, 2.45, and 1.63 mA cm^{-2} to modifications with CoPi, FePi, and NiPi, respectively. However, it is noted an exponential decay of the j_{pc} in the first 300 s, after that, average decay rates of -1.72×10^{-7}, -2.33×10^{-7}, and -1.75×10^{-7} A s^{-1} were shown by the heterojunctions containing CoPi, FePi, and NiPi, respectively. Although the catalyst FePi presents a high decay rate it did not exhibit the high loss of activity over the experiment time. At the end of the stability experiment were observed j_{pc} around 0.45, 0.82, and 0.43 mA cm^{-2} to the photoanodes $WO_3/BiVO_4$/CoPi, $WO_3/BiVO_4$/FePi, and $WO_3/BiVO_4$/NiPi, respectively, which correspond to loss of 60.8, 66.5, and 73.6% of the initial j_{pc}. The experiments with 3 replicates showed a variation of ± 15, 17, and 11% in the values of final j_{pc} to CoPi, FePi, and NiPi PED, respectively. The decrease in the activity of the catalyst is an inherent problem associated with $BiVO_4$ photocorrosion and loss of catalyst materials due to agitation or dissolution, once the water oxidation produces protons.[15] To each oxygen molecule is produced 4 protons in the same reaction site, which cause a huge decrease in the local pH and, consequently, attacks the catalyst and even the light-absorbing layer.[39] There are strategies to try to overcome this issue as the use of low bias to stability test, the use of slightly alkaline buffer electrolyte, or the use of self-regeneration catalyst.[16] Nevertheless, the catalysts show a significant increase in the j_{pc} even though it was used a simple methodology to their PED. It remains to be seen the structural changes that occurred after the catalysts PED.

Figure 5 shows the XRD pattern to the substrate FTO and the other modifications after deposition of each new layer. It is possible to assign all diffraction peaks in the samples to the monoclinic $BiVO_4$ (JPDS PDF 44-81), monoclinic WO_3 (JPDS PDF 43-1035), and tetragonal SnO_2 (JPDS PDF 41-1445) crystalline phases. The peaks at 15.2°, 19.0°, and 30.7° are characteristics of the monoclinic $BiVO_4$, while the peak at 24.4° is a feature of the monoclinic WO_3. However, in agreement with the XRD pattern, the WO_3 presents a preferential growth in the (200) direction, once the peak at 24.4° shows a higher intensity than the ones in 23.1° and 23.6°. There are no peaks of crystalline phases attributed to the catalysts PED on $WO_3/BiVO_4$, which indicates that the catalysts are deposited

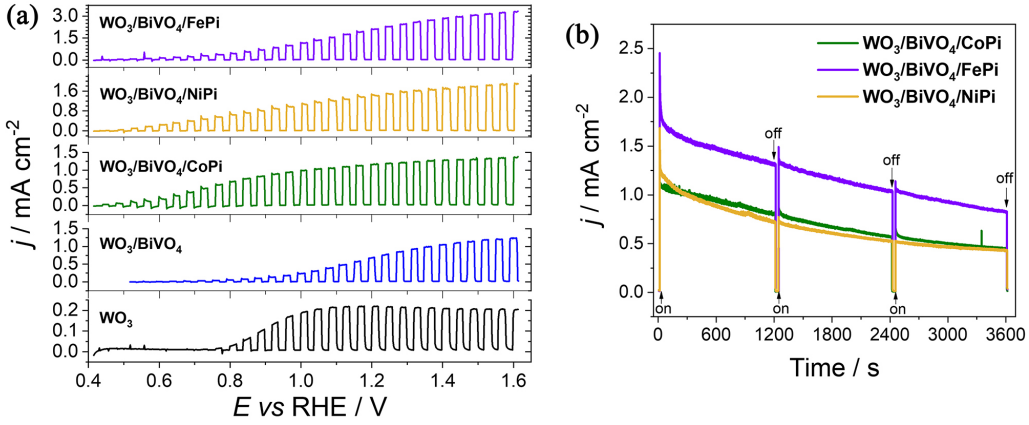

Figure 4. (a) Linear voltammetry at 10 mV s^{-1} into 0.5 mol L^{-1} Na_2SO_4 + 0.1 mol L^{-1} Na_2HPO_4 pH 7.0, under chopped light. (b) Stability of the photoanodes at 1.23 V *vs*. RHE. Xenon lamp, 100 W, filter AM 1.5 G, irradiance 100 mW cm^{-2}.

as amorphous compounds. The peaks at 37.9°, 51.8°, 61.7°, 65.8°, and 78.6° are ascribed to SnO_2.

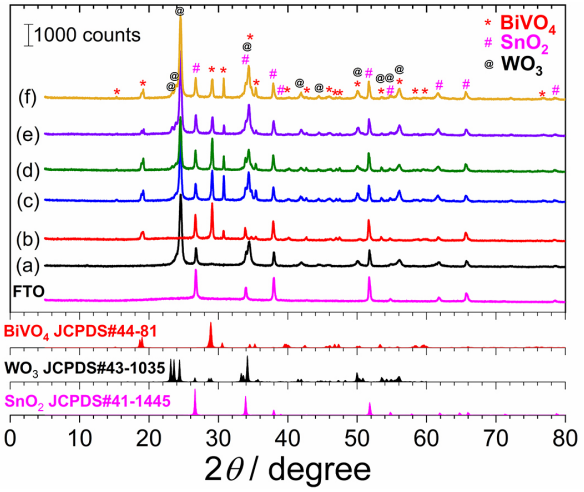

Figure 5. XRD patterns of the samples (a) pristine WO_3, (b) pristine $BiVO_4$, (c) $WO_3/BiVO_4$, (d) $WO_3/BiVO_4$/CoPi, (e) $WO_3/BiVO_4$/FePi, and (f) $WO_3/BiVO_4$/NiPi. The symbols identify the peaks referring to the crystalline phases of (∗) $BiVO_4$, (@) WO_3, and (#) SnO_2.

Figure 6A shows the Raman scattering spectrum where is noted characteristic scattering peaks for monoclinic WO_3 at 130, 264, 322, 704, and 801 cm^{-1}.[40,41] The intense peaks at 704 and 801 cm^{-1} correspond to stretch vibrations and angular deformation of the W–O–W bond, respectively. The peaks at 264 and 322 cm^{-1} refer to the angular vibration modes of the O–W–O bond, while the peak at 130 cm^{-1} corresponds to the lattice vibration of the crystal. For $BiVO_4$, scattering peaks are observed at 122, 203, 324, 359, 710, and 826 cm^{-1}, which correspond to crystal vibration modes (122 and 203 cm^{-1}), angular deformations of the tetrahedral VO_4^{-III} (324 and 359 cm^{-1}), and stretching in the V–O bonds (707 and 826 cm^{-1}).[42] For the heterojunction containing the investigated catalysts (CoPi, FePi, and NiPi) no Raman scattering peak is observed for their oxides or phosphates. The thin films are opaque, therefore diffuse reflectance spectroscopy was used as an optical analysis technique. The spectra are shown in Figure 6B and the differences between the heterojunction before and after the OECs deposition are related to the scattering baseline and opacity of the film. The deposition of the OECs does not change the bandgap, since there is no decrease in the reflectance due to their presence.

The bandgap energy seems not to be affected by the catalyst PED too. Figures 6C and 6D show the Tauc plot assuming an indirect and direct electronic transition between valence and conduction band. In the indirect transition, the bandgap is estimated by the extrapolation to axis *x* (hν, photon energy obtained by the product between Planck constant and frequency of the incident radiation, respectively) at the point where the baseline and the straight line that marks the increase of light absorption intersects (the

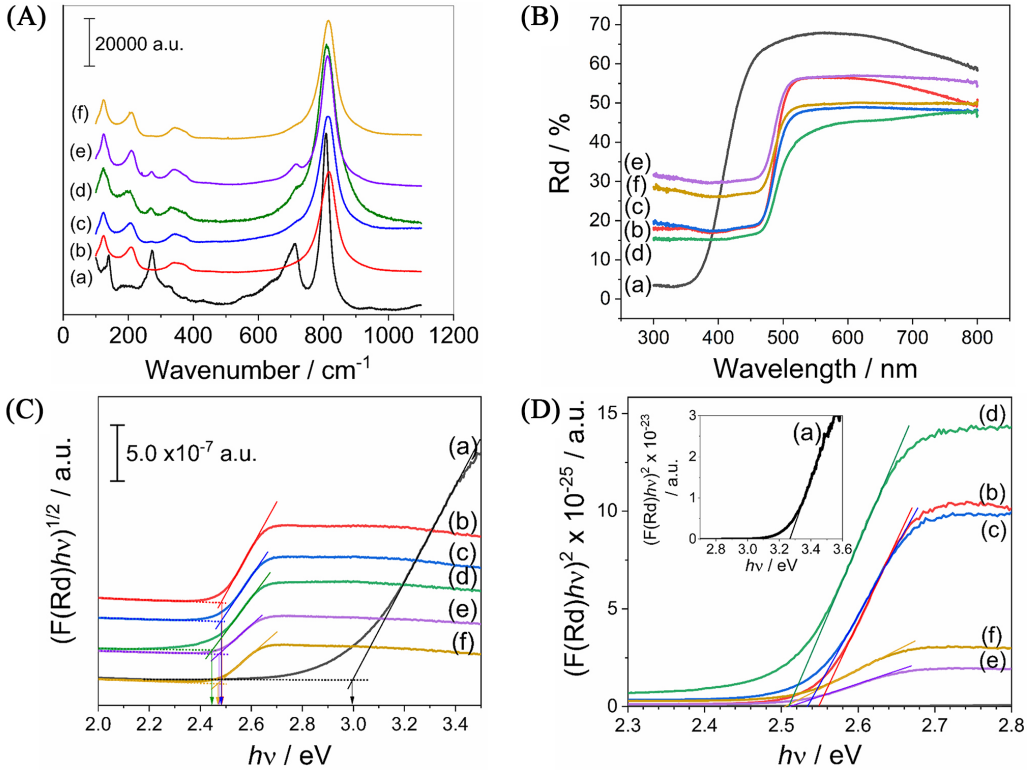

Figure 6. (A) Raman shift, (B) DRS, and Tauc plot considering (C) an indirect and (D) a direct electronic transition of the samples (a) pristine WO_3, (b) pristine $BiVO_4$, (c) $WO_3/BiVO_4$, (d) $WO_3/BiVO_4$/CoPi, (e) $WO_3/BiVO_4$/FePi, and (f) $WO_3/BiVO_4$/NiPi.

arrow pointed to the axis *x*). On the other hand, the direct bandgap is calculated by the extrapolation of the straight line that marks the increase of light absorption to the axis *x* (hν).[43] The bandgap values are shown in Table 1, where can be noted no significant changes in the value of band gap either for direct or indirect transition after deposition of $BiVO_4$ on WO_3 or even after catalysts PED on heterojunction $WO_3/BiVO_4$. However, the indirect bandgap expected to monoclinic WO_3 is around 2.8 eV, but here it was estimated a value of 3.00 eV.[40,41] It is believed that the preferential growth of the (200) crystalline plane changed the bandgap energy of pristine WO_3. In addition, as the technique used for the evaluation of bandgap was the diffuse reflectance spectroscopy, after the $BiVO_4$ deposition, the light-absorbing layer with the lowest bandgap overlaps the absorption of those with high bandgap energy. Thus, in the $WO_3/BiVO_4$ heterojunction is shown just the bandgap energy of the $BiVO_4$ layer, which is around 2.5 eV to monoclinic $BiVO_4$.[44,45]

Table 1. Bandgap energies estimated to the photoanodes

Photoanode	Direct bandgap / eV	Indirect bandgap / eV
WO_3	3.26	3.00
$BiVO_4$	2.55	2.48
$WO_3/BiVO_4$	2.53	2.48
$WO_3/BiVO_4$/CoPi	2.51	2.44
$WO_3/BiVO_4$/FePi	2.51	2.47
$WO_3/BiVO_4$/NiPi	2.50	2.47

According to the microscopy images, shown in Figure 7, seems that the $BiVO_4$ layer, in the $WO_3/BiVO_4$ heterostructure, assumes columnar structures as reported by Coelho *et al.*[10] (insert of Figure 7a). This occurs because the electrodeposition of metallic Bi growth particles in a pyramidal shape, which drives the morphology of the $BiVO_4$ during the heat treatment in presence of NH_4VO_4. The particles in all samples are near-spherical shape and the average size of the $BiVO_4$ particles on WO_3 film on the heterojunction is 209 ± 55 nm, nevertheless, after CoPi PED it is observed particles of 630 ± 188 nm. The CoPi seems to uniformly coat the $WO_3/BiVO_4$ film, creating a compact catalytic layer that reduces the "texture" of the previously formed columnar structures (Figure 7b). Furthermore, it is observed a cracked clay morphology only in the sample $WO_3/BiVO_4$/CoPi, similar to that related by Kanan and Nocera.[34] In contrast, the FePi PED suggests dissolving the columnar structure of the $BiVO_4$ layer and covering the remaining particles with a thin layer of FePi catalyst (Figure 7c). Interestingly, the size of the particles is 215 ± 74 nm, near the $BiVO_4$ particles in the heterostructure without the catalysts. Finally, in Figure 7d it is shown the SEM images of the NiPi PED, which keeps the same columnar morphology presented by the heterostructure and a particle size of 228 ± 60 nm. Even so, the surface texturing and the formation of the desired co-catalytic layer are evident in the insert of Figure 7d.

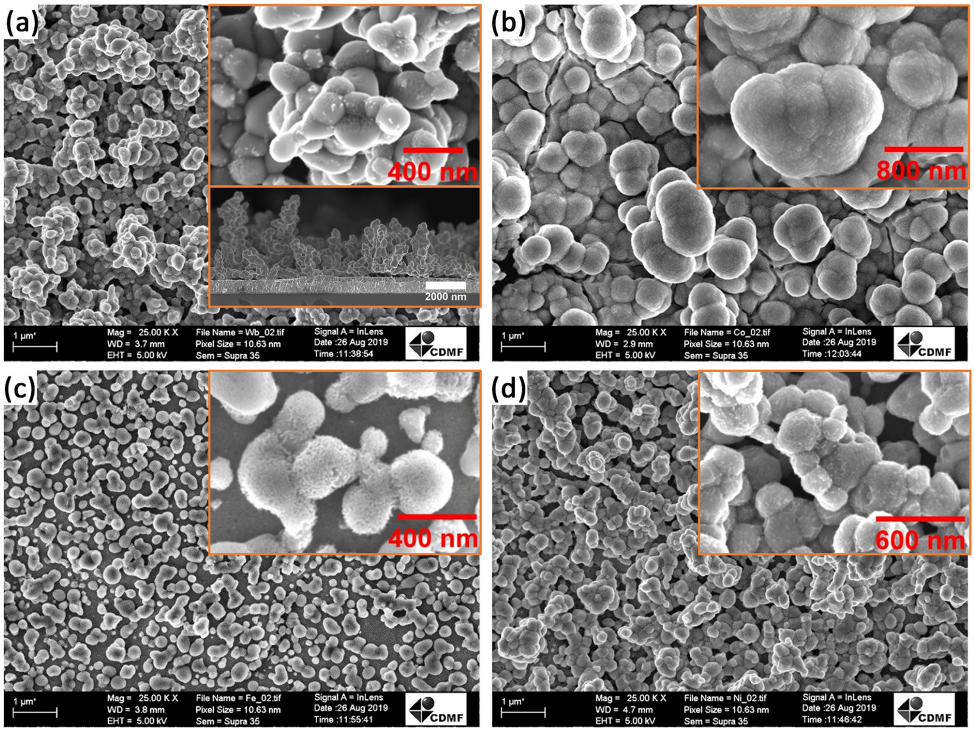

Figure 7. SEM images of the samples (a) $WO_3/BiVO_4$, (b) $WO_3/BiVO_4$/CoPi, (c) $WO_3/BiVO_4$/FePi, and (d) $WO_3/BiVO_4$/NiPi.

The presence of an uneven texture on $WO_3/BiVO_4$ heterojunction is a characteristic of the catalyst deposition as shown in the reports using FeOOH or NiOOH as co-catalyst.[26,28,30,31,37] As the catalyst PED occurs *in situ* the nucleation produces particles with a dimension of few nanometers, which turns the photoanode surface rougher. Even though the huge increase in the j_{pc} is the strongest evidence of the success in the PED of the catalyst.

Conclusions

The $WO_3/BiVO_4$ heterojunction was built using a methodology of spray deposition, electrodeposition, and heat treatment showing an increase in the j_{pc} about 3.4 times related to pristine WO_3 (0.22 mA cm^{-2}). However, the photoelectrodeposition (PED) of the oxygen-evolving catalysts based on oxy-hydroxide phosphates of Co, Fe, and Ni enhanced 1.56, 2.83, and 1.89 times the j_{pc} when compared to the $WO_3/BiVO_4$ without the catalysts. The highest value of j_{pc} was reached with FePi catalyst (2.12 mA cm^{-2}). The optimization of the catalyst deposition showed more positive effects on the j_{pc} under incident illumination during the PED, which indicates that the presence of light induces the deposition of the catalysts preferentially at active sites. Regarding the optical and crystalline characterization, no changes were observed either in the X-ray diffraction patterns and Raman scattering or in the bandgap energy of the heterojunction containing the catalysts. However, the morphology was greatly affected by the FePi and CoPi PED. In the first, the procedure seemed to dissolve the columnar structures of $BiVO_4$ and to cover the remaining particles with a thin layer of the catalyst while in the second, it was generated a film on the $BiVO_4$ layer. Further, the NiPi PED does not significantly change the heterostructure morphology and just covers the surface of the photoanode. Therefore, the performances obtained to the photoanodes here from the use of easily scalable and low-cost techniques, such as electrodeposition and spray, prove to be competitive and promising compared to complex and costly processes for reducing the effects of charge recombination at the bulk and the interface photoanode-electrolyte aiming water splitting.

Acknowledgments

This work was supported by the National Council of Technological and Scientific Development (CNPq), Brazil, by the São Paulo Research Foundation (FAPESP), Brazil, CEPID grant No. 2013/07296-2, and by the FAPESP/SHELL grant No. 2017/11986-5 and No. 2021/08614-4.

References

1. Kamat, P. V.; *J. Phys. Chem. C* **2007**, *111*, 2834.
2. Razykov, T. M.; Ferekides, C. S.; Morel, D.; Stefanakos, E.; Ullal, H. S.; Upadhyaya, H. M.; *Sol. Energy* **2011**, *85*, 1580.
3. McKone, J. R.; Lewis, N. S.; Gray, H. B.; *Chem. Mater.* **2014**, *26*, 407.
4. Li, D.; Shi, J.; Li, C.; *Small* **2018**, *14*, 1704179.
5. Yang, W.; Moon, J.; *ChemSusChem* **2019**, *12*, 1889.
6. Tahir, M.; Pan, L.; Idrees, F.; Zhang, X.; Wang, L.; Zou, J. J.; Wang, Z. L.; *Nano Energy* **2017**, *37*, 136.
7. Lee, S. A.; Choi, S.; Kim, C.; Yang, J. W.; Kim, S. Y.; Jang, H. W.; *ACS Mater. Lett.* **2020**, *2*, 107.
8. Park, Y.; McDonald, K. J.; Choi, K. S.; *Chem. Soc. Rev.* **2013**, *42*, 2321.
9. Kalanoor, B. S.; Seo, H.; Kalanur, S. S.; *Mater. Sci. Energy Technol.* **2018**, *1*, 49.
10. Coelho, D.; Gaudêncio, J. P. R. S.; Carminati, S. A.; Ribeiro, F. W. P.; Nogueira, A. F.; Mascaro, L. H.; *Chem. Eng. J.* **2020**, *399*, 125836.
11. Kim, J. H.; Jo, Y.; Kim, J. H.; Jang, J. W.; Kang, H. J.; Lee, Y. H.; Kim, D. S.; Jun, Y.; Lee, J. S.; *ACS Nano* **2015**, *9*, 11820.
12. Rettie, A. J. E.; Lee, H. C.; Marshall, L. G.; Lin, J. F.; Capan, C.; Lindemuth, J.; McCloy, J. S.; Zhou, J.; Bard, A. J.; Mullins, C. B.; *J. Am. Chem. Soc.* **2013**, *135*, 11389.
13. Abdi, F. F.; Savenije, T. J.; May, M. M.; Dam, B.; Van De Krol, R.; *J. Phys. Chem. Lett.* **2013**, *4*, 2752.
14. Ding, C.; Shi, J.; Wang, Z.; Li, C.; *ACS Catal.* **2017**, *7*, 675.
15. Kuang, Y.; Jia, Q.; Ma, G.; Hisatomi, T.; Minegishi, T.; Nishiyama, H.; Nakabayashi, M.; Shibata, N.; Yamada, T.; Kudo, A.; Domen, K.; *Nat. Energy* **2017**, *2*, 16191.
16. Tayebi, M.; Lee, B. K.; *Renewable Sustainable Energy Rev.* **2019**, *111*, 332.
17. Lin, R.; Wan, J.; Xiong, Y.; Wu, K.; Cheong, W. C.; Zhou, G.; Wang, D.; Peng, Q.; Chen, C.; Li, Y.; *J. Am. Chem. Soc.* **2018**, *140*, 9078.
18. Reier, T.; Nong, H. N.; Teschner, D.; Schlögl, R.; Strasser, P.; *Adv. Energy Mater.* **2017**, *7*, 1601275.
19. Spöri, C.; Kwan, J. T. H.; Bonakdarpour, A.; Wilkinson, D. P.; Strasser, P.; *Angew. Chem., Int. Ed.* **2017**, *56*, 5994.
20. Kim, J. H.; Jang, J. W.; Kang, H. J.; Magesh, G.; Kim, J. Y.; Kim, J. H.; Lee, J.; Lee, J. S.; *J. Catal.* **2014**, *317*, 126.
21. Liu, K.; Zhang, C.; Sun, Y.; Zhang, G.; Shen, X.; Zou, F.; Zhang, H.; Wu, Z.; Wegener, E. C.; Taubert, C. J.; Miller, J. T.; Peng, Z.; Zhu, Y.; *ACS Nano* **2018**, *12*, 158.
22. Chemelewski, W. D.; Lee, H. C.; Lin, J. F.; Bard, A. J.; Mullins, C. B.; *J. Am. Chem. Soc.* **2014**, *136*, 2843.
23. Chemelewski, W. D.; Rosenstock, J. R.; Mullins, C. B.; *J. Mater. Chem. A* **2014**, *2*, 14957.

24. Lim, H.; Kim, J. H. J. Y.; Evans, E. J.; Rai, A.; Kim, J. H. J. Y.; Wygant, B. R.; Mullins, C. B.; *ACS Appl. Mater. Interfaces* **2017**, *9*, 30654.
25. Roger, I.; Shipman, M. A.; Symes, M. D.; *Nat. Rev. Chem.* **2017**, *1*, 3.
26. de Araújo, M. A.; Coelho, D.; Mascaro, L. H.; Pereira, E. C.; *J. Solid State Electrochem.* **2018**, *22*, 1539.
27. Chhetri, M.; Dey, S.; Rao, C. N. R.; *ACS Energy Lett.* **2017**, *2*, 1062.
28. Wang, S.; He, T.; Yun, J. H.; Hu, Y.; Xiao, M.; Du, A.; Wang, L.; *Adv. Funct. Mater.* **2018**, *28*, 1802685.
29. Shi, Y.; Yu, Y.; Yu, Y.; Huang, Y.; Zhao, B.; Zhang, B.; *ACS Energy Lett.* **2018**, *3*, 1648.
30. Seabold, J. A.; Choi, K. S.; *J. Am. Chem. Soc.* **2012**, *134*, 2186.
31. Kim, T. W.; Choi, K.-S.; *Science* **2014**, *343*, 990.
32. Abdi, F. F.; van de Krol, R.; *J. Phys. Chem. C* **2012**, *116*, 9398.
33. Abdi, F. F.; Firet, N.; van de Krol, R.; *ChemCatChem* **2013**, *5*, 490.
34. Kanan, M. W.; Nocera, D. G.; *Science* **2008**, *321*, 1072.
35. Lide, D. R.; Mohr, P. J.; Taylor, B. N.; Martienssen, W.; *CRC Handbook of Chemistry and Physics*, vol. 1, 88th ed.; Lide, D. R., ed.; Taylor & Francis Group: Boca Raton, 2007.
36. Mascaro, L. H.; Pockett, A.; Mitchels, J. M.; Peter, L. M.; Cameron, P. J.; Celorrio, V.; Fermin, D. J.; Sagu, J. S.; Wijayantha, K. G. U.; Kociok-Köhn, G.; Marken, F.; *J. Solid State Electrochem.* **2014**, *19*, 31.
37. McDonald, K. J.; Choi, K. S.; *Energy Environ. Sci.* **2012**, *5*, 8553.
38. Moniz, S. J. A.; Shevlin, S. A.; Martin, D. J.; Guo, Z. X.; Tang, J.; *Energy Environ. Sci.* **2015**, *8*, 731.
39. Huynh, M. H. V.; Meyer, T. J.; *Chem. Rev.* **2007**, *107*, 5004.
40. Ramana, C. V.; Utsunomiya, S.; Ewing, R. C.; Julien, C. M.; Becker, U.; *J. Phys. Chem. B* **2006**, *110*, 10430.
41. Díaz-Reyes, J.; Castillo-Ojeda, R.; Galván-Arellano, M.; Zaca-Moran, O.; *Adv. Condens. Matter Phys.* **2013**, *2013*, ID 591787.
42. Galembeck, A.; Alves, O. L.; *Thin Solid Films* **2000**, *365*, 90.
43. Nowak, M.; Kauch, B.; Szperlich, P.; *Rev. Sci. Instrum.* **2009**, *80*, 046107.
44. Han, L.; Abdi, F. F.; van de Krol, R.; Liu, R.; Huang, Z.; Lewerenz, H. J.; Dam, B.; Zeman, M.; Smets, A. H. M.; *ChemSusChem* **2014**, *7*, 2832.
45. Brack, P.; Sagu, J. S.; Peiris, T. A. N.; McInnes, A.; Senili, M.; Wijayantha, K. G. U.; Marken, F.; Selli, E.; *Chem. Vap. Deposition* **2015**, *21*, 41.

Submitted: November 6, 2021
Published online: January 18, 2022